Diffraction of Radio Waves from Arbitrary One-Dimensional Surface Impedance Discontinuities

Kamal Sarabandi, *Senior Member, IEEE*, and Mark D. Casciato, *Member, IEEE*

***Abstract*— Characterization of a propagation channel is essential in developing an optimum wireless system. Accurate prediction of field parameters, both stochastic and deterministic can greatly reduce the time and effort required to design and develop a progression of prototypes necessary to achieve the final system requirements. To accomplish this, a physics-based methodology must be considered. In this methodology, a series of scattering and diffraction models must be developed and integrated which accurately represent the effects of various terrain features on electromagnetic wave propagation. In this paper, diffraction of electromagnetic waves from a surface impedance discontinuity, which can represent a river or trough is considered. In order to more accurately represent the transmitter antenna, dipole excitation is used as the wave source. The river or trough is modeled as a variable impedance insert in an infinite plane with one-dimensional (1-D) variation. An integral equation for an impedance surface is formulated in the Fourier domain, which is solved iteratively using a perturbation technique. An analytical solution is provided to any desired order in terms of multifold convolution integrals of the Fourier transform of the impedance function. The far-field integral is then evaluated using the stationary phase technique. Next, the formulation is extended to a short dipole with arbitrary orientation by expanding the dipole field in terms of a continuous spectrum of plane waves. Results are then shown for both plane wave and dipole excitation. Scattering results for an impedance insert are generated up to second order. These results are then compared to geometrical theory of diffraction (GTD) results. The effect of varying both the width and perturbation parameter of the insert are described. Results from plane wave incidence at various oblique angles are shown. Effects of varying the impedance transition shape are shown and compared. Scattering results for dipole excitation show E-field components in a planar grid at a given height above the scattering plane. It is shown that the $\hat{z}$ component of the diffracted field is maximized for either a vertical or horizontal dipole orientation. Effects generated by varying the receiver height are also discussed.**

***Index Terms*— Diffraction, impedance discontinuity, surface impedance.**

I. Introduction

DUE to the rapid growth of wireless technology, the accurate prediction of both deterministic and stochastic processes involved in the propagation of electromagnetic waves in a communications channel has attained prominence in recent years [1]–[4]. Simplistic statistical-based channel models, while providing some insight, are not based on the physics of the problem and, therefore, do not work well in a dynamic environment with both significant terrain and environmental changes. Because of this, improved scattering and diffraction models for terrestrial and man-made targets must be developed to accurately predict the performance of a wireless system. In an environment where line-of-sight propagation is not dominant, multipath signals caused by scattering and diffraction establish the communications link between receiver and transmitter. Dispersion and fading are important features of such communication channels, which influence the performance of advanced spread spectrum modulation schemes. With this in mind, a physics-based methodology is being considered to develop and integrate advanced scattering models for various terrain and environmental features, such as mountains and hills, buildings, rough surfaces, surface discontinuities, vegetation (trees), atmospheric propagation effects, etc.

The problem of plane wave diffraction from shorelines in planar land–sea boundaries using the Wiener–Hopf technique, was addressed by Bazer *et al*. [5]. For this problem, the sea and land surfaces were modeled by a perfectly conducting and impedance surface, respectively, and the diffraction is evaluated using the Wiener–Hopf method. Wait and others addressed the diffraction effects caused by an inhomogeneous surface using an integral equation technique to solve for an attenuation factor [6]–[8]. The solution is formulated in terms of complex integrals that must be solved numerically. In this paper, an analytical formulation is developed to predict the diffraction from a surface impedance discontinuity of an arbitrary profile such as rivers, shorelines, or troughs when excited by a small dipole of arbitrary orientation. Basically, the river is modeled as an impedance change in an infinite impedance plane, representing the ground plane, which is an acceptable approximation over a frequency range including high-frequency (HF) to lower microwave frequencies. An integral equation is developed and then solved analytically using a perturbation technique, assuming a one-dimensional (1-D) impedance variation. For noncanonical problems, it is usually difficult to obtain exact solutions for Maxwell's equations and, thus, approximate solutions are sought. Geometrical theory of diffraction (GTD) methods, while accurate at high frequencies, have only been applied to problems where abrupt variations in a surface are present. A solution is sought for problems with a more general variation across the diffraction surface with arbitrary dimensions compared to the wavelength. When the actual solution of a problem varies only slightly (is perturbed) from a known exact solution perturbation theory is a viable approach to solve these general problems. An

Manuscript received July 10, 1997; revised July 13, 1998. This work was supported by the U.S. Army Research Office under contract DAAH04-96-1-0377.

The authors are with the Radiation Laboratory, Department of Electrical Engineering and Computer Science, University of Michigan, Ann Arbor, MI 48109 USA.

Publisher Item Identifier S 0018-926X(99)02211-5.

integral equation, which assumes a phase variation only in the dimension where the impedance is constant, is formulated in the Fourier domain for plane wave excitation. In [9], it was shown that an integral formulation for a resistive sheet with resistivity $R(x)$ could be extended to an impedance sheet by simply replacing $R(x)$ with $\eta(x)/2$, where $\eta(x)$ describes the impedance variation of the surface. From this, recursive expressions for the induced current of any order, for arbitrary impedance variations, are derived. Far-field expressions for plane wave excitation are derived by applying stationary phase to evaluate the radiation integral. Due to the nature of the far-field expression the induced current is left in the Fourier domain, thus eliminating the need for additional integration. The derivation is then extended to the small dipole excitation. Scattered field expressions are formulated by applying the spectral-domain representation of the dipole fields. For source and observation many wavelengths distant stationary phase is used to evaluate the field expression integrals. Results are then shown for both plane wave and dipole illuminations. Results up to second order are generated for plane wave excitation across a step insert and compared to a third order GTD solution [10]. An error bound for the perturbation parameter is established and defined in terms of incident wave polarization and angle. The effects of varying both the perturbation parameter and insert width are discussed. Results are then given for plane wave excitation at various oblique angles. Results from both an impedance step insert and a more gradual impedance transition, better representing a riverbed, are compared. Results from dipole excitation show a two-dimensional (2-D) grid of receiver field strengths for both vertical and horizontal dipole orientation. Results show that the $\hat{z}$ component of the diffracted field is maximized for either a vertically or horizontally oriented dipole.

II. Integral Equation Formulation for Variable Impedance Surfaces

The geometry of the problem is as shown in Fig. 1 with θ and ϕ as defined in standard spherical coordinates. Note that the geometry is not a function of y and, thus, the induced current along y and the scattered field are of the form $e^{ik_y^i y}$ or are in phase with the incident field. We start by defining the impedance boundary condition on the scattering surface as

$$\hat{n} \times (\hat{n} \times \mathbf{E}) = -\eta(x)(\hat{n} \times \mathbf{H}). \tag{1}$$

Applying the field equivalence principle [11] to (1), the magnetic field is replace by an equivalent electric current and a magnetic wall placed behind the current, doubling it. The following implied integral equation, which describes the tangential surface electric fields, is generated:

$$\mathbf{E}^t = (\mathbf{E}^i + \mathbf{E}^r + \mathbf{E}^s)|_{z=0} = \eta(x)\mathbf{J}(x). \tag{2}$$

The scattered field on the impedance surface is defined by

$$\mathbf{E}^s = 2ik_0 Z_0 \int_{-\infty}^{+\infty} \overline{\overline{G}}_{2D\perp}(\boldsymbol{\rho}, \boldsymbol{\rho}') \bullet \mathbf{J}(x')\, dx' \tag{3}$$

where the factor of 2 in (3) is from image theory and $\overline{\overline{G}}_{2D\perp}(\boldsymbol{\rho}, \boldsymbol{\rho}')$ is the spectral domain representation of the 2-D

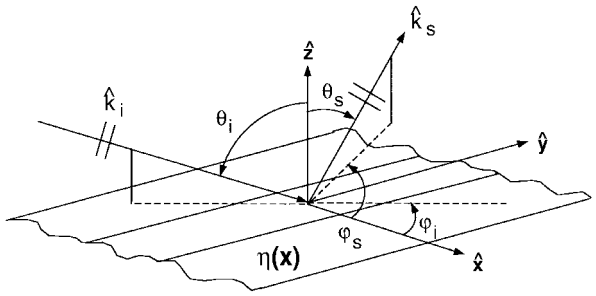

Fig. 1. Scattering geometry for variable impedance surface.

Dyadic Green's function for $z > z'$, derived from the spectral domain representation of the free-space Dyadic Green's function. To obtain (3), we start with the spectral domain form of the free-space dyadic Green's function for $z > z'$ given by [12]

$$\overline{\overline{G}}(\mathbf{r}, \mathbf{r}') = -\hat{z}\hat{z}\frac{\delta(r-r')}{k_0^2} + \frac{i}{8\pi^2}\iint \frac{1}{k_z}\left[\overline{\overline{I}} - \frac{\mathbf{kk}}{k_0^2}\right] \cdot e^{i(k_x(x-x')+k_y(y-y')+k_z(z-z'))}\, dk_x\, dk_y \tag{4}$$

where $\mathbf{k} = k_x\hat{x} + k_y\hat{y} + k_z\hat{z}$. Since the dependence of the induced currents and fields on y is known ($e^{ik_y^i y}$), the 2-D Green's function can be evaluated from (4) by integrating out the y dimension. Noting that $[\overline{\overline{I}} - (\mathbf{kk}/k_0^2)] = [\overline{\overline{I}} - \hat{k}\hat{k}] = [\hat{e}\hat{e} + \hat{m}\hat{m}]$ and integrating out the y dimension gives the following form of the 2-D Dyadic Green's function for $z > z'$:

$$\overline{\overline{G}}_{2D\perp}(\boldsymbol{\rho}, \boldsymbol{\rho}') = e^{ik_y^i y}\frac{i}{4\pi}\int \frac{1}{k_z}[\hat{e}\hat{e} + \hat{m}\hat{m}]e^{ik_x(x-x')}\, dk_x. \tag{5}$$

In (5), $\boldsymbol{\rho} = x\hat{x} + z\hat{z}$ and $k_z = \sqrt{k_0^2 - k_y^{i2} - k_x^2} = \sqrt{k_0^2 \sin^2\beta - k_x^2}$ with β defined by $\hat{k}^i \cdot \hat{y} = \cos\beta = \sin\theta_i \sin\phi_i$. The unit vectors $\hat{e}$ and $\hat{m}$ in (5) are defined by

$$\hat{e} = \frac{\hat{k} \times \hat{y}}{|\hat{k} \times \hat{y}|} \quad \text{and} \quad \hat{m} = \hat{e} \times \hat{k}. \tag{6}$$

Noting that $\hat{k} = [k_x\hat{x} + k_y\hat{y} + k_z\hat{z}]/k_0$, simplified expressions for $\hat{e}$ and $\hat{m}$ are given by

$$\hat{e} = \frac{k_x\hat{z} - k_z\hat{x}}{k_0 \sin\beta} \quad \text{and} \quad \hat{m} = \frac{\hat{y} - \cos\beta\hat{k}}{\sin\beta}. \tag{7}$$

In (3), $\mathbf{J}(x') = J_x(x')\hat{x} + J_y(x')\hat{y}$ and a dependency on y of the form $e^{ik_y^i y}$ is assumed and suppressed. Substituting (5) into (3) it can be shown that

$$\mathbf{E}^s = -2\frac{k_0 Z_0}{4\pi}\int_{-\infty}^{+\infty}\frac{1}{k_z}\left\{\hat{e}\left[J_x(x')\left(\frac{-k_z}{k_0 \sin\beta}\right)\right] + \hat{m}\left[-\cot\beta\frac{k_x}{k_0}J_x(x') + \sin\beta sp J_y(x')\right]\right\} \cdot e^{ik_x(x-x')}\, dk_x\, dx'. \tag{8}$$

The incident field is now defined as $\mathbf{E}^i = \mathbf{E}_0 e^{i\hat{k}^i \cdot \mathbf{r}}$ and from this the tangential incident and reflected fields on the surface are

$$(\mathbf{E}^i_{\tan} + \mathbf{E}^r_{\tan})|_{z=0} = 2(\mathbf{E}_0 - (\mathbf{E}_0 \cdot \hat{z})\hat{z})e^{i(k_x^i x + k_y^i y)} \tag{9}$$

where again the factor of two on the right side of (9) is from image theory. The explicit integral equation can now be written as

$$\frac{\eta(x)}{2}\mathbf{J}(x) = (\mathbf{E}_0 - (\mathbf{E}_0 \cdot \hat{z})\hat{z})e^{ik_x^i x} - \frac{k_0 Z_0}{4\pi} \cdot \iint_{-\infty}^{+\infty} \frac{1}{k_z}\left\{\left[\hat{e}\left[J_x(x')\left(\frac{-k_z}{k_0 \sin\beta}\right)\right]\right.\right. + \hat{m}\left[-\cot\beta\frac{k_x}{k_0}J_x(x') + \sin\beta sp J_y(x')\right]\left.\right\} \cdot e^{ik_x(x-x')}\, dk_x\, dx'. \quad (10)$$

Fourier transforming the integral equation and invoking the convolution theorem of Fourier transforms [13] eliminates the integration with respect to x' in scattered field term of (10). The Fourier transform of the scattered field term creates a $\delta(\alpha - k_x)$ term allowing the final integration with respect to k_x to be evaluated algebraically, modifying k_z to $k_z = \sqrt{k_0^2 \sin^2\beta - \alpha^2}$. Performing these operations on (10) generates the following integral equation in the Fourier domain:

$$\frac{1}{4\pi}\eta(\alpha) * \tilde{J}_x(\alpha) = (\mathbf{E}_0 - (\mathbf{E}_0 \bullet \hat{z})\hat{z})2\pi\delta(\alpha - k_x^i) - \frac{k_0 Z_0}{2} \cdot \frac{1}{k_z}\left\{\hat{e}\left[\frac{-k_z}{k_0 \sin\beta}\tilde{J}_x(\alpha)\right] + \hat{m}\left[-\cot\beta\frac{\alpha}{k_0}\tilde{J}_x(\alpha) + \sin\beta sp\tilde{J}_y(\alpha)\right]\right\}. \quad (11)$$

Now using the definitions for $\hat{e}$ and $\hat{m}$ given in (7) and after some algebraic manipulations, the following integral equations for each current component in the Fourier domain are obtained:

$$\frac{1}{4\pi}\eta(\alpha) * \tilde{J}_x(\alpha) = (\mathbf{E}_0 \bullet \hat{x})2\pi\delta(\alpha - k_x^i) - \frac{k_0 Z_0}{2} \cdot \frac{1}{k_z}\left\{\left(1 - \frac{\alpha^2}{k_0^2}\right)\tilde{J}_x(\alpha) - \cos\beta\frac{\alpha}{k_0}\tilde{J}_y(\alpha)\right\} \quad (12)$$

$$\frac{1}{4\pi}\eta(\alpha) * \tilde{J}_y(\alpha) = (\mathbf{E}_0 \bullet \hat{y})2\pi\delta(\alpha - k_x^i) - \frac{k_0 Z_0}{2} \cdot \frac{1}{k_z}\left\{-\cos\beta\frac{\alpha}{k_0}\tilde{J}_x(\alpha) + \sin^2\beta sp\tilde{J}_y(\alpha)\right\}. \quad (13)$$

III. Iterative Solution

In this section, a recursive relation will be shown relating any order current to the previous order current. The zeroth order current components ($\tilde{J}_{0x}$ and $\tilde{J}_{0y}$), which produce the reflected field, will first be derived and then the recursive relationship will be shown. Definitions for the surface impedance and induced current expansions must first be given. The surface impedance is defined as

$$\eta(x) = \eta_0(1 + \Delta h(x)) \quad (14)$$

where Δ is the perturbation parameter. In the Fourier domain (14) becomes

$$\tilde{\eta}(\alpha) = 2\pi\eta_0\delta(\alpha) + \eta_0\tilde{h}(\alpha)\Delta. \quad (15)$$

For sufficiently small values of Δ the surface currents in the Fourier domain may be expanded as

$$\tilde{\mathbf{J}}(\alpha) = \sum_{n=0}^{\infty}(\tilde{J}_{nx}(\alpha)\hat{x} + \tilde{J}_{ny}(\alpha)\hat{y})\Delta^n. \quad (16)$$

For the zeroth order current components, $\tilde{J}_{0x}, \tilde{J}_{0y}$, corresponding to $\Delta = 0, \tilde{\eta}(\alpha) = 2\pi\eta_0\delta(\alpha)$. Performing the convolution on the left sides of (12) and (13) gives the following two integral equations for the x and y components of the surface fields:

$$\frac{1}{2}\eta_0\tilde{J}_{0x}(\alpha) = 2\pi E_{0x}\delta(\alpha - k_x^i) - \frac{k_0 Z_0}{2} \cdot \frac{1}{k_z}\left\{\left(1 - \frac{\alpha^2}{k_0^2}\right)\tilde{J}_{0x} - \cos\beta\frac{\alpha}{k_0}\tilde{J}_{0y}(\alpha)\right\} \quad (17)$$

$$\frac{1}{2}\eta_0\tilde{J}_{0y}(\alpha) = 2\pi E_{0y}\delta(\alpha - k_x^i) - \frac{k_0 Z_0}{2} \cdot \frac{1}{k_z}\left\{-\cos\beta\frac{\alpha}{k_0}\tilde{J}_{0x}(\alpha) + \sin^2\beta sp\tilde{J}_{0y}(\alpha)\right\}. \quad (18)$$

Collecting terms in (17) and (18) and solving for $\tilde{J}_{0x}, \tilde{J}_{0y}$ gives (19) and (20), shown at the bottom of the page, for the zeroth order currents. The recursive relationship for higher order currents is derived by applying the perturbed impedance of (15) and the current expansion of (16) to (12) giving the following integral equation relating $\tilde{J}_{nx}(\alpha)$ to the higher order

$$\tilde{J}_{0x}(\alpha) = \frac{\left\{E_{0x}\left[\frac{1}{2}\eta_0 + \frac{k_0 Z_0}{2k_z}\sin^2\beta\right] + E_{0y}\left[\frac{Z_0\alpha}{2k_z}\cos\beta\right]\right\}2\pi\delta(\alpha - k_x^i)}{\left[\frac{1}{2}\eta_0 + \frac{k_0 Z_0}{2k_z}\left(1 - \frac{\alpha^2}{k_0^2}\right)\right]\left[\frac{1}{2}\eta_0 + \frac{k_0 Z_0}{2k_z}\sin^2\beta\right] - \left(\frac{Z_0\alpha\cos\beta}{2k_z}\right)^2} \quad (19)$$

$$\tilde{J}_{0y}(\alpha) = \frac{\left\{E_{0y}\left[\frac{1}{2}\eta_0 + \frac{k_0 Z_0}{2k_z}\left(1 - \frac{\alpha^2}{k_0^2}\right)\right] + E_{0x}\left[\frac{Z_0\alpha}{2k_z}\cos\beta\right]\right\}2\pi\delta(\alpha - k_x^i)}{\left[\frac{1}{2}\eta_0 + \frac{k_0 Z_0}{2k_z}\left(1 - \frac{\alpha^2}{k_0^2}\right)\right]\left[\frac{1}{2}\eta_0 + \frac{k_0 Z_0}{2k_z}\sin^2\beta\right] - \left(\frac{Z_0\alpha\cos\beta}{2k_z}\right)^2} \quad (20)$$

x, y current components:

$$\sum_{n=0}^{\infty}\left(\frac{1}{2}\eta_0\tilde{J}_{nx}(\alpha)\Delta^n+\frac{1}{4\pi}\eta_0\tilde{h}(\alpha)*\tilde{J}_{nx}(\alpha)\Delta^{n+1}\right)$$
$$=2\pi E_{0x}\delta(\alpha-k_x^i)-\frac{k_0Z_0}{2}\sum_{n=0}^{\infty}\frac{1}{k_z}\cdot\left\{\left(1-\frac{\alpha^2}{k_0^2}\right)\tilde{J}_{nx}(\alpha)-\cos\beta\frac{\alpha}{k_0}\tilde{J}_{ny}(\alpha)\right\}\Delta^n. \quad (21)$$

Rearranging the terms gives

$$\frac{1}{2}\eta_0\tilde{J}_{0x}(\alpha)+\sum_{n=0}^{\infty}\left(\frac{1}{2}\eta_0(\tilde{J}_{(n+1)x}(\alpha)+\frac{1}{2\pi}\tilde{h}(\alpha)*\tilde{J}_{nx}(\alpha)\right)\Delta^{n+1}$$
$$=2\pi E_{0x}\delta(\alpha-k_x^i)-\frac{k_0Z_0}{2}\frac{1}{k_z}\cdot\left\{\left(1-\frac{\alpha^2}{k_0^2}\right)\tilde{J}_{0x}(\alpha)-\cos\beta\frac{\alpha}{k_0}\tilde{J}_{0y}(\alpha)\right\}-\frac{k_0Z_0}{2}\sum_{n=0}^{\infty}\frac{1}{k_z}\cdot\left\{\left(1-\frac{\alpha^2}{k_0^2}\right)\tilde{J}_{(n+1)x}(\alpha)-\cos\beta\frac{\alpha}{k_0}\tilde{J}_{(n+1)y}(\alpha)\right\}\cdot\Delta^{n+1}. \quad (22)$$

Observing that (17) is embedded in (22) all terms containing zero order current components vanish. Noting that the equality remaining must hold for all orders of Δ, the following recursive current relationship is established for the x current component:

$$\frac{1}{2}\eta_0\tilde{J}_{(n+1)x}(\alpha)=-\frac{1}{4\pi}\eta_0\tilde{h}(\alpha)*\tilde{J}_{nx}(\alpha)-\frac{k_0Z_0}{2}\frac{1}{k_z}\cdot\left\{\left(1-\frac{\alpha^2}{k_0^2}\right)\tilde{J}_{(n+1)x}(\alpha)-\cos\beta\frac{\alpha}{k_0}\tilde{J}_{(n+1)y}(\alpha)\right\}. \quad (23)$$

Similarly, the integral equation relating $\tilde{J}_{ny}(\alpha)$ to the higher order currents is

$$\frac{1}{2}\eta_0\tilde{J}_{(n+1)y}(\alpha)=-\frac{1}{4\pi}\eta_0\tilde{h}(\alpha)*\tilde{J}_{ny}(\alpha)-\frac{k_0Z_0}{2}\frac{1}{k_z}\cdot\left\{-\cos\beta\frac{\alpha}{k_0}\tilde{J}_{(n+1)x}(\alpha)+\sin^2\beta\tilde{J}_{(n+1)y}(\alpha)\right\}. \quad (24)$$

Collecting terms and solving (23) and (24) for the higher order current components gives the recursive relationship between each current order and the previous order shown in (25) and (26) at the bottom of the page, where

$$\sin^2\beta=1-\left(\frac{k_y^i}{k_0}\right)^2,\quad \cos\beta=\frac{k_y^i}{k_0},\qquad \text{and}$$
$$k_z=\sqrt{k_0^2-\alpha^2-k_y^{i2}}. \quad (27)$$

IV. Far-Field Evaluation

Once the induced currents are obtained, the scattered field expression can be derived analytically for any order current provided the observation point is many wavelengths from the scatterer. Recalling that the induced current is of the form $\mathbf{J}_n(x,y)=\Delta^n\mathbf{J}_n(x)e^{ik_y^iy}$, the scattered field can be obtained from

$$\mathbf{E}^s(\mathbf{r}_s)=2ik_0Z_0\Delta^n\int_{-\infty}^{+\infty}\int\overline{\overline{G}}(\mathbf{r}_s,\mathbf{r}')\cdot\mathbf{J}_n(x')e^{ik_y^iy'}\,dx'\,dy' \quad (28)$$

where $\overline{\overline{G}}(\mathbf{r}_s,\mathbf{r}')$ in (28) is the spectral-domain representation of the free-space dyadic Green's function for $z>z'$ given in (4). Upon substitution of (4) into (28) and integrating first with respect to y' and then k_y gives

$$\mathbf{E}^s(\mathbf{r}_s)=-\frac{k_0Z_0\Delta^n}{2\pi}\int_{-\infty}^{+\infty}\int\frac{1}{k_z}e^{i(k_xx_s+k_y^iy_s+k_zz_s)}\{\hat{h}\hat{h}+\hat{v}\hat{v}\}\bullet\mathbf{J}_n(x')e^{ik_xx'}\,dx'\,dk_x. \quad (29)$$

The unit vectors $\hat{h},\hat{v}$ in (29) are given by

$$\hat{h}=\frac{\mathbf{k}\times\hat{z}}{|\mathbf{k}\times\hat{z}|}=\frac{-k_\rho^i\cos\psi_s\hat{y}+k_y^i\hat{x}}{\sqrt{k_\rho^{i2}\cos^2\psi_s+k_y^{i2}}}=\frac{-k_\rho^i\cos\psi_s\hat{y}+k_y^i\hat{x}}{\sqrt{k_0^2\cos^2\psi_s+k_y^{i2}\sin^2\psi_s}} \quad (30)$$

and (31), shown at the bottom of the next page. Noting that $\int_{-\infty}^{+\infty}\mathbf{J}_n(x')e^{ik_xx'}\,dx'$ is simply the Fourier transform of $\mathbf{J}_n(x')$ with $\alpha=k_x$ the final form of the scattered field in

$$\tilde{J}_{(n+1)x}(\alpha)=\frac{1}{2\pi}\left[\frac{\left(\frac{k_z\eta_0}{k_0Z_0}\right)\left[\left(\frac{k_z\eta_0}{k_0Z_0}\right)+\sin^2\beta\right]\tilde{h}(\alpha)*\tilde{J}_{nx}(\alpha)+\frac{k_z\eta_0}{k_0Z_0}\frac{\alpha}{k_0}\cos\beta sp\tilde{h}(\alpha)*\tilde{J}_{ny}(\alpha)}{\left(1+\frac{k_z\eta_0}{k_0Z_0}\right)\left\{\frac{\alpha^2}{k_0^2}-\sin^2\beta-\frac{k_z\eta_0}{k_0Z_0}\right\}}\right] \quad (25)$$

$$\tilde{J}_{(n+1)y}(\alpha)=\frac{1}{2\pi}\left[\frac{\left(\frac{k_z\eta_0}{k_0Z_0}\right)\left[\left(\frac{k_z\eta_0}{k_0Z_0}\right)+\left(1-\frac{\alpha^2}{k_0^2}\right)\right]\tilde{h}(\alpha)*\tilde{J}_{ny}(\alpha)+\frac{k_z\eta_0}{k_0Z_0}\frac{\alpha}{k_0}\cos\beta sp\tilde{h}(\alpha)*\tilde{J}_{nx}(\alpha)}{\left(1+\frac{k_z\eta_0}{k_0Z_0}\right)\left\{\frac{\alpha^2}{k_0^2}-\sin^2\beta-\frac{k_z\eta_0}{k_0Z_0}\right\}}\right] \quad (26)$$

the far zone is

$$\mathbf{E}^s(\mathbf{r}_s) = -\frac{k_0 Z_0 \Delta^n}{2\pi} \int_{-\infty}^{+\infty} \{\hat{h}\hat{h} + \hat{v}\hat{v}\} \bullet \tilde{\mathbf{J}}_n(k_x) \frac{e^{i(k_x x_s + k_y^i y_s + k_z z_s)}}{\sqrt{k_0^2 - k_x^2 - k_y^{i^2}}}\, dk_x. \tag{32}$$

In the far field for $\rho_s = \sqrt{x_s^2 + z_s^2} \gg \lambda$, stationary phase can be used to evaluate the integral in (32) [14]. Evaluating the exponential function $f(k_x) = k_x x_s + k_z z_s$ at it's extrema gives the following stationary phase point:

$$k_{xsp} = \sqrt{k_0^2 - k_y^{i^2}} \cos\psi_s \triangleq k_\rho^i \cos\psi_s. \tag{33}$$

Here, ρ_s and ψ_s are the radial scattering distance and scattering angle from the x axis respectively in the $x - z$ plane with $k_z = k_\rho^i \sin\psi_s$, k_ρ^i simply the propagation vector k_0 projected into the $x-z$ plane or $k_\rho^i = k_0 \sin\beta$. Applying stationary phase for a 1-D integral [14] to (32) gives the following far-zone scattered-field expression for plane wave excitation:

$$\mathbf{E}_n^s(\mathbf{r}_s) = -\frac{k_0 Z_0 \Delta^n}{\sqrt{2\pi k_\rho^i \rho_s}} \{\hat{h}\hat{h} + \hat{v}\hat{v}\} \bullet \tilde{\mathbf{J}}_n(k_\rho^i \cos\psi_s) \cdot e^{i(k_\rho^i \rho_s - (\pi/4))} e^{ik_y^i y_s}. \tag{34}$$

V. Evaluation of Scattered Field for Short Dipole Excitation

In this section, the scattering formulation for an impedance insert excited at oblique incidence will be extended to include dipole excitation. Consider a short dipole of length l carrying a sinusoidal current of amplitude I and located at $\mathbf{r}_0 = x_0\hat{x} + y_0\hat{y} + z_0\hat{z}$. The field emitted from this dipole at some observation point $\mathbf{r} = x\hat{x} + y\hat{y} + z\hat{z}$ for $z < z_0$ can be represented by a continuous spectrum of plane waves. The form of this field is expressed by

$$\mathbf{E}_d(\mathbf{r}) = \frac{-ilk_0 Z_0}{8\pi^2} \iint_{-\infty}^{+\infty} \left\{ \frac{1}{k_z^i} \left[\bar{\bar{I}} - \frac{\mathbf{K}^i \mathbf{K}^i}{k_0^2} \right] \bullet \hat{l} e^{-i\mathbf{K}^i \cdot \mathbf{r}_0} \right\} \cdot e^{i\mathbf{K}^i \cdot \mathbf{r}}\, dk_x^i\, dk_y^i \tag{35}$$

where $\mathbf{k}^i = k_x^i\hat{x} + k_y^i\hat{y} - k_z^i\hat{z}, k_z^i = \sqrt{k_0^2 - k_x^{i^2} - k_y^{i^2}}$, and $\hat{l}$ is the unit vector along the short dipole. The integrand of (35) can be restated as $\mathbf{E}_0 e^{i\mathbf{K}^i \cdot (\mathbf{r} - \mathbf{r}_0)}$, where

$$\mathbf{E}_0 = \frac{-ilk_0 Z_0}{8\pi^2} \frac{1}{k_z^i} \left[\hat{l} - \frac{\mathbf{K}^i \bullet \hat{l}\mathbf{K}^i}{k_0^2} \right]. \tag{36}$$

Recognizing that the integrand describes a plane wave propagating along $\mathbf{K}^i/k_0$ and using the linearity property of electromagnetic waves, the scattered field can be expressed by a superposition of scattering from individual plane waves or

$$\mathbf{E}_{dn}^s(\mathbf{r}_s) = \iint_{-\infty}^{+\infty} \mathbf{D}(\mathbf{K}^i) e^{ik_\rho^i \rho_s} e^{ik_y^i y_s} e^{-i\mathbf{K}^i \cdot \mathbf{r}_0}\, dk_x^i\, dk_y^i \tag{37}$$

where

$$\mathbf{D}(\mathbf{K}^i) = \frac{-k_0 Z_0 \Delta^n}{\sqrt{2\pi k_\rho^i \rho_s}} \{\hat{h}\hat{h} + \hat{v}\hat{v}\} \bullet \tilde{\mathbf{J}}_n(k_\rho^i \cos\psi_s) e^{-i(\pi/4)} \tag{38}$$

and $\mathbf{D}(\mathbf{K}^i) e^{ik_\rho^i \rho_s} e^{ik_y^i y_s}$ in (37) is the scattered far field from each individual plane wave as described by (34). Again, considering a situation where distance between source and observation are large compared to wavelength, stationary phase is used to evaluate the 2-D integral of (37) [15]. Noting that the exponential function is given by

$$f(k_x^i, k_y^i) = k_y^i(y_s - y_0) - k_x^i x_0 + k_z^i z_0 + \sqrt{k_0^2 - k_y^{i^2}}\, \rho_s \tag{39}$$

the stationary phase points are found to be

$$\begin{aligned} k_{xsp}^i &= \frac{-x_0(\rho_s + \rho_0)}{\rho_0 R} k_0 \\ k_{ysp}^i &= \frac{(y_s - y_0)}{R} k_0 \\ k_{zsp}^i &= \frac{z_0(\rho_s + \rho_0)}{\rho_0 R} k_0 \end{aligned} \tag{40}$$

where $\rho_0 = \sqrt{x_0^2 + z_0^2}$ and $R = \sqrt{(y_s - y_0)^2 + (\rho_s + \rho_0)^2}$. Evaluating (37) at the stationary phase points gives the final form of the scattered electric field for the small dipole or

$$\mathbf{E}_{dn}^s(\mathbf{r}_s) = \mathbf{D}(\mathbf{K}_{SP}^i) \frac{2\pi i}{C} e^{ik_0 R} \tag{41}$$

where $\mathbf{K}_{sp}^i$ is $\mathbf{K}^i$ evaluated at the stationary phase point given by (40) and where

$$C = \sqrt{\frac{\partial^2 f}{\partial k_x^{i^2}} \frac{\partial^2 f}{\partial k_y^{i^2}} - \left(\frac{\partial^2 f}{\partial k_x^i \partial k_y^i} \right)^2}. \tag{42}$$

The second derivatives at the stationary phase point are given by

$$\frac{\partial^2 f}{\partial k_x^{i^2}} = -\frac{\rho_0^2}{z_0 k_{zsp}^i} \tag{43}$$

$$\frac{\partial^2 f}{\partial k_y^{i^2}} = -\frac{k_{zsp}^{i^2} + k_{ysp}^{i^2}}{k_{zsp}^{i^3}} z_0 - \frac{k_0^2}{[k_0^2 - k_{ysp}^{i^2}]^{3/2}} \rho_s \tag{44}$$

$$\frac{\partial^2 f}{\partial k_x^i \partial k_y^i} = -\frac{k_{xsp}^i k_{ysp}^i}{k_{zsp}^{i^3}} z_0. \tag{45}$$

$$\hat{v} = \frac{1}{k_0}\hat{h} \times \mathbf{k} = \frac{-k_\rho^i k_y^i \sin\psi_s \hat{y} - k_\rho^{i^2} \sin\psi_s \cos\psi_s \hat{x} + (k_0^2 \cos^2\psi_s + k_y^{i^2} \sin^2\psi_s)\hat{z}}{k_0 \sqrt{k_0^2 \cos^2\psi_s + k_y^{i^2} \sin^2\psi_s}} \tag{31}$$

Substituting the expression for $\mathbf{D}(\mathbf{K}^i_{SP})$ from (38) into (41) and noting that k^i_ρ at the stationary phase point $k^i_{\rho sp} = ((\rho_s+\rho_0)/R)k_0$ gives the following analytical expression for the scattered field:

$$\mathbf{E}^s_{dn}(\mathbf{r}_s) = \frac{-iZ_0\Delta^n}{C}\sqrt{\frac{2\pi k_0 R}{(\rho_s+\rho_0)\rho_s}}e^{ik_0R} \cdot\{\hat{h}_{SP}\hat{h}_{SP}+\hat{v}_{SP}\hat{v}_{SP}\} \bullet \tilde{\mathbf{J}}_n\left(k_0\frac{(\rho_s+\rho_0)}{R}\cos\psi_s\right)e^{-i(\pi/4)}. \quad (46)$$

In (46), the unit vectors $\hat{h}_{SP}$ and $\hat{v}_{SP}$ are those given by (30) and (31) evaluated at the stationary phase point. The following expression must be used for the plane wave incident field amplitude which is implicit in $\tilde{\mathbf{J}}_n(\alpha)$:

$$\mathbf{E}_0 = \frac{-IlZ_0}{8\pi^2}\frac{\rho_0 R}{z_0(\rho_s+\rho_0)}\left\{\hat{l}-\frac{\mathbf{K}^i\bullet\hat{l}}{k_0^2}\mathbf{K}^i\right\} \quad (47)$$

where $\mathbf{K}^i = (k_0/R)(-((\rho_s+\rho_0)/\rho_0)x_0\hat{x}+(y_s-y_0)\hat{y}-((\rho_s+\rho_0)/\rho_0)z_0\hat{z})$. Simplified expressions for $\tilde{\mathbf{J}}_n(\alpha)$, where $\alpha = k_0\sin\beta\cos\psi_s$ can be derived by evaluating (25) and (26) at the stationary phase points and making the substitutions $\sin\beta = ((\rho_s+\rho_0)/R), \cos\beta = (y_s-y_0/R)$ and $k_z = k_0\sin\beta\sin\psi_s$ giving (48) and (49), shown at the bottom of the page.

Evaluating (19) and (20) at the stationary phase point gives the following explicit expressions for the zeroth order currents:

$$\tilde{J}_{0x}(\alpha) = \frac{2z_0(\rho_s+\rho_0)}{\rho_0 R}\cdot\frac{\left[\frac{E_{0x}}{Z_0}\left(\frac{\eta_0}{Z_0}+\frac{\rho_0(\rho_s+\rho_0)}{z_0R}\right)-\frac{E_{0y}}{Z_0}\frac{x_0(y_s-y_0)}{z_0R}\right]}{\left[1+\frac{\eta_0}{Z_0}\frac{z_0(\rho_s+\rho_0)}{\rho_0R}\right]\left[\frac{z_0(\rho_s+\rho_0)}{\rho_0R}+\frac{\eta_0}{Z_0}\right]}\cdot 2\pi\delta\left(\alpha+\frac{k_0(\rho_s+\rho_0)x_0}{\rho_0R}\right) \quad (50)$$

and (51), shown at the bottom of the page, where E_{0x} and E_{0y} are derived from (47) and are given as

$$E_{0x} = -\frac{IlZ_0}{8\pi^2}\frac{\rho_0R}{z_0(\rho_s+\rho_0)}\left[l_x+\frac{\mathbf{K}^i\bullet\hat{l}x_0(\rho_s+\rho_0)}{k_0\rho_0R}\right] \quad (52)$$

$$E_{0y} = -\frac{IlZ_0}{8\pi^2}\frac{\rho_0R}{z_0(\rho_s+\rho_0)}\left[l_y-\frac{\mathbf{K}^i\bullet\hat{l}(y_s-y_0)}{k_0R}\right] \quad (53)$$

with $\hat{l} = l_x\hat{x}+l_y\hat{y}+l_z\hat{z}$ and $\mathbf{K}^i$ as defined previously. Now, defining the zeroth order currents as

$$\tilde{J}_{0x}(\alpha) = U_{0x}2\pi\delta\left(\alpha+\frac{k_0x_0(\rho_s+\rho_0)}{\rho_0R}\right)$$
$$\tilde{J}_{0y}(\alpha) = U_{0y}2\pi\delta\left(\alpha+\frac{k_0x_0(\rho_s+\rho_0)}{\rho_0R}\right) \quad (54)$$

and substituting into (48) and (49), (55) and (56), shown at the bottom of the next page, are obtained as the explicit expressions for the first order currents, which can be used in (46) to find the first order diffracted fields.

VI. Results

In this section, the analytical results based on the perturbation solution are validated in the limiting cases and are compared with those obtained from independent techniques where possible. As discussed previously, diffraction due to plane wave excitation will first be examined. Then, a numerical example is considered, to demonstrate the diffracted field distribution caused by a river for a dipole excitation. For both plane wave and dipole excitations the reference impedance value is chosen to be $\eta_0 = 20.9015 - i17.4433$, where η_0 is the value of the unperturbed impedance. As the impedance transition is designed to model a river, the value of η_0 is selected to simulate the impedance of moist soil surrounding the river bed. The value is arrived at by assuming the impedance of the river is modeled by slightly saline water at 25 °C. Assuming the saline content of the water is approximately 4 pp/1000, where pp/1000 is defined as parts per 1000 on

$$\tilde{J}_{(n+1)x}(\alpha) = -\frac{1}{2\pi}\frac{\frac{\eta_0}{Z_0}\sin\beta\left\{\left[\frac{\eta_0}{Z_0}\sin\psi_s+\sin\beta\right]\tilde{h}(\alpha)*\tilde{J}_{nx}(\alpha)+\cos\psi_s\cos\beta sp\tilde{h}(\alpha)*\tilde{J}_{ny}(\alpha)\right\}}{\left(1+\frac{\eta_0}{Z_0}\sin\beta\sin\psi_s\right)\left(\frac{\eta_0}{Z_0}+\sin\beta\sin\psi_s\right)} \quad (48)$$

$$\tilde{J}_{(n+1)y}(\alpha) = -\frac{1}{2\pi}\frac{\frac{\eta_0}{Z_0}\left\{\left[\frac{\eta_0}{Z_0}\sin\beta\sin\psi_s+1-\sin^2\beta\cos^2\psi_s\right]\tilde{h}(\alpha)*\tilde{J}_{ny}(\alpha)+\sin\beta\cos\beta\cos\psi_s sp\tilde{h}(\alpha)*\tilde{J}_{nx}(\alpha)\right\}}{\left(1+\frac{\eta_0}{Z_0}\sin\beta\sin\psi_s\right)\left(\frac{\eta_0}{Z_0}+\sin\beta\sin\psi_s\right)} \quad (49)$$

$$\tilde{J}_{0y}(\alpha) = \frac{2z_0(\rho_s+\rho_0)}{\rho_0R}\frac{\left[\frac{E_{0y}}{Z_0}\left(\frac{\eta_0}{Z_0}+\frac{\rho_0R}{z_0(\rho_s+\rho_0)}\left(1-\frac{x_0^2}{\rho_0^2}\frac{(\rho_s+\rho_0)^2}{R^2}\right)\right)-\frac{E_{0x}}{Z_0}\frac{x_0(y_s-y_0)}{z_0R}\right]}{\left[1+\frac{\eta_0}{Z_0}\frac{z_0(\rho_s+\rho_0)}{\rho_0R}\right]\left[\frac{z_0(\rho_s+\rho_0)}{\rho_0R}+\frac{\eta_0}{Z_0}\right]}2\pi\delta\left(\alpha+\frac{k_0(\rho_s+\rho_0)x_0}{\rho_0R}\right) \quad (51)$$

a weight basis, the river impedance, at 30 MHz is found to be $\eta_r = 13.9343 - i11.6289$, derived from the equations for complex permittivity given by Ulaby *et al.*, for saline water [16]. The soil impedance value is then assumed to be 1.5 times that of the river or $20.9015 - i17.4433$, corresponding to a perturbation parameter Δ of 0.5. This value corresponds closely to the value of $20.43 - i19.27$, derived from the values of permittivity and conductivity given by Hipp [17] for San Antonio Gray Loam with a 5% gravimetric moisture content and a density of 1.6 g/cm^3.

Note that Fig. 1, shown previously, describes the scattering coordinates for both types of excitation.

A. Plane Wave Excitation

In this section, results will be shown and discussed for plane wave excitation of the impedance surface. Initially, the impedance transition will be modeled as a step discontinuity. The step insert will be used to validate and characterize the method by comparing with a GTD solution, normal incidence ($\beta = \pi/2$). Results will then be shown for various oblique incidence angles. A more gradual impedance transition function, which better represents an actual riverbed, will then be described and results compared with that of the step insert. Note that all plane wave results show the normalized scattering width σ_s/λ around the specular scattering cone with $\sigma_s = 2\pi\rho(|\mathbf{E}_s|/|\mathbf{E}_i|)$ as $\rho \to \infty$. The specular cone is the cone generated by the requirement that the scattered field propagation vector along the uniform axis of the insert matches that of the incident field along the insert [see (32)]. In the plotted results, θ_s varying from -90 to 90° is equivalent to ψ_s in (33) varying from 180 to 0°.

An important feature of the perturbation solution is its convergence properties. It is important to know for what values of Δ the perturbation expansion of (16) converges to the exact solution. To characterize the limits of the perturbation method an error bound must be established on the maximum Δ allowable, at a given incidence angle and for a particular impedance profile. Mathematically, this can be shown by finding the radius of convergence of the expanded current series, in terms of the perturbation parameter Δ. Even for a value of $\Delta > 1$ the series will converge if the current coefficients are decreasing for higher orders. Let us first consider a limiting case for which an exact solution exists. This corresponds to a constant perturbation function ($h(x) = 1$) whose Fourier transform is a δ function. Applying this to (19) and (20) and assuming $\beta = \pi/2$ gives the following forms for the horizontally and vertically polarized currents:

$$\mathbf{J}_{0h}(x) = \frac{[\sin\phi_i\hat{x} + \cos\phi_i\hat{y}]}{\frac{1}{2}\eta_0(1+\Delta) + \frac{Z_0}{2\cos\theta_i}} e^{ik_0\sin\theta_i(\cos\phi_i x + \sin\phi_i y)} \tag{57}$$

$$\mathbf{J}_{0v}(x) = [\cos\phi_i\hat{x} + \sin\phi_i\hat{y}] \frac{\cos\theta_i}{\frac{1}{2}\eta_0(1+\Delta) + \frac{Z_0\cos\theta}{2}} \cdot e^{ik_0\sin\theta_i(\cos\phi_i x + \sin\phi_i y)} \tag{58}$$

After some algebra the previous equations can be put in the form

$$\mathbf{J}_{0h,v}(x) = K\frac{1}{\xi}\cdot\frac{1}{1+\frac{\Delta}{\xi}} \tag{59}$$

where K are constants and

$$\xi = \begin{cases} \dfrac{Z_0}{\eta_0\cos\theta_i} + 1, & \text{for } \mathbf{J}_{0h}(x) \\ \dfrac{Z_0\cos\theta_i}{\eta_0} + 1, & \text{for } \mathbf{J}_{0v}(x). \end{cases} \tag{60}$$

The Taylor Series expansion of (59) will converge uniformly for all $\Delta < \xi$, which indicates that the radius of convergence for low-impedance surfaces can be very high. Using the value for moist soil given previously or $\eta_0 = 20.9015 - i17.4433$, the limiting cases are for $\theta_i = 0$ and $\theta_i = \pi/2$. For horizontal polarization this gives the maximum values for Δ of 14.62, for $\theta_i = 0$ and ∞, for $\theta_i = \pi/2$, and for vertical polarization 14.62 and 1, respectively. Note that for all plane wave results that follow $\theta_i = 45°$ indicating that $\Delta < 20.265$ and $\Delta < 10.57$ for horizontal and vertical polarization, respectively, is acceptable for our study.

Having established a sense of the radius of convergence of the perturbation solution, it is also desirable to know at what Δ a first-order solution will give desirable accuracy. With this in mind, results were generated for both first- and second-order diffraction using the perturbation method and compared to a third-order GTD solution for the step-impedance function. The order of the GTD solution describes to what degree diffracted fields are accounted for. First order are the diffracted fields generated by the incident wave, second order are the diffracted fields generated by these initial diffracted fields interacting with the diffracting edges, etc. TM results are shown for Δ varying from 1.0 to 5.0, in Fig. 3. Note that TM and TE are

$$\tilde{J}_{1x}(\alpha) = -\frac{\frac{\eta_0}{Z_0}\sin\beta\left\{\left[\frac{\eta_0}{Z_0}\sin\psi_s + \sin\beta\right]U_{0x} + \cos\psi_s\cos\beta U_{0y}\right\}\tilde{h}\left(\alpha + \frac{k_0(\rho_s+\rho_0)x_0}{\rho_0 R}\right)}{\left(1+\frac{\eta_0}{Z_0}\sin\beta\sin\psi_s\right)\left(\frac{\eta_0}{Z_0}+\sin\beta\sin\psi_s\right)} \tag{55}$$

$$\tilde{J}_{1y}(\alpha) = -\frac{\frac{\eta_0}{Z_0}\left\{\left[\frac{\eta_0}{Z_0}\sin\beta\sin\psi_s + 1 - \sin^2\beta\cos^2\psi_s\right]U_{0y} + \sin\beta\cos\beta\cos\psi_s U_{0x}\right\}\tilde{h}\left(\alpha + \frac{k_0(\rho_s+\rho_0)x_0}{\rho_0 R}\right)}{\left(1+\frac{\eta_0}{Z_0}\sin\beta\sin\psi_s\right)\left(\frac{\eta_0}{Z_0}+\sin\beta\sin\psi_s\right)} \tag{56}$$

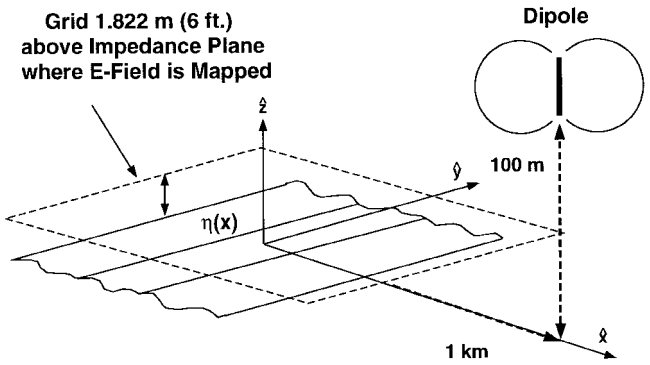

Fig. 2. Dipole position over variable impedance plane.

defined as transverse to the plane of incidence. All results shown are for a step insert 5λ wide at normal incidence ($\beta = \pi/2$). As can be seen, for a Δ of up to 2.5 the first-order perturbation solution tracks the GTD very nicely for the TM case except at near grazing. The perturbation results begin to degrade for the TM case for a Δ of 5.0. The TM results shown are a worst case with first- and second-order TE results showing excellent agreement for a Δ as high as 5.0.

The convergence property of the perturbation solution as a function of the width of the insert step function was also observed. The insert width was varied from 1 to 20λ. Δ was fixed at 2.5, where the first-order TM solution was shown previously to degrade for an insert width of 5λ. Both the TM and TE results were basically insensitive to insert width variations.

Having characterized the perturbation method, both in terms of an error bound and insert width, results will now be shown for a step insert 5λ wide with $\eta_0 = 20.9015 - i17.4433$ and $\Delta = 0.5$ excited at oblique incidence angles. As described previously these parameters best characterize those of an actual river surrounded by soil. The insert width was chosen to correspond to a river 50 m wide at 30 MHz.

Both copolarization and cross-polarization results are shown in Fig. 4. Fig. 4(a) shows the copolarization scattering width, normalized to wavelength (σ_s/λ), for TM case of a step insert excited by a plane wave at a constant angle $\theta_i = 45°$ with ϕ_i rotated at the oblique angles, 0, 45, and 90°. Referring to Fig. 4(a), the peak scattering for $\phi_i = 0°$ is shown to be at approximately the specular angle of $\theta_s = 45°$. At $\phi_i = 90°$ the incident wave is along the step insert and the scattering pattern is symmetric in the x-z plane as expected.

Theoretically no cross-polarization results can exist for an incidence angle of $\phi_i = 0$. As ϕ_i is rotated toward 90° cross-polarization levels become more significant. Fig. 4(b) shows cross-polarization results, again in terms of normalized scattering width for plane wave excitation with $\theta_i = 45°$ and $\phi_i = 90°$. Note that as the incident field is rotated to a position along the step insert $\phi_i = 90°$, the cross-polarization levels rise, and, in fact, the cross-polarization for $\mathrm{TE}_{\mathrm{TM}}$ with $\phi_i = 90°$ is the highest level for all results including copolarization curves. This indicates that receiver polarization (measuring the diffracted field) need be adjusted for optimum polarization matching as the incident field propagation vector moves about the step insert.

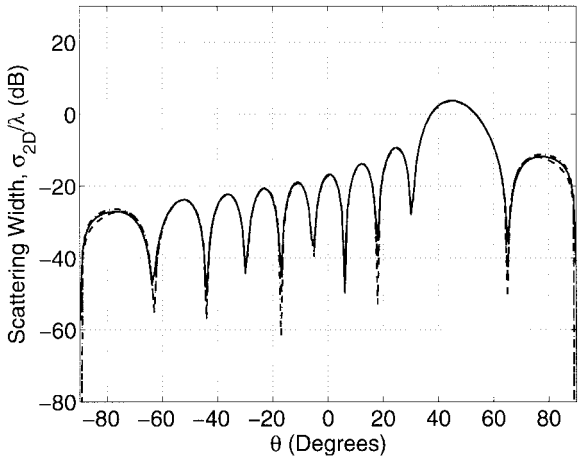

(a)

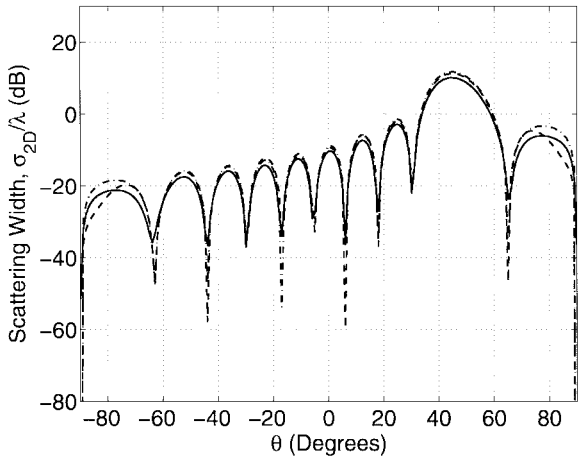

(b)

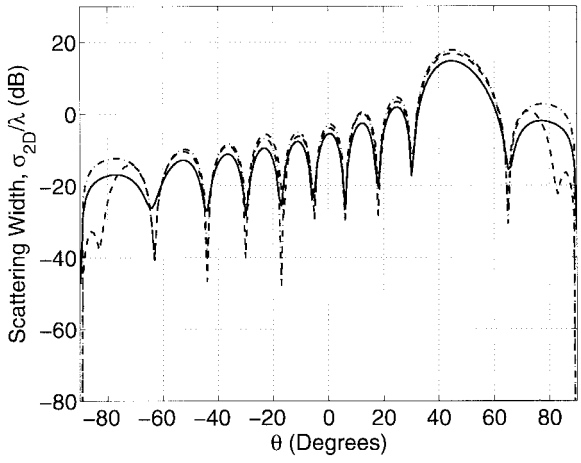

(c)

Fig. 3. Normalized bistatic echo width (σ_s/λ) of an impedance step insert 5λ wide with $\eta_o = 20.9015 - i17.4433$, at $\theta_i = 45°$, $\phi_i = 0°$, first (- · - · - ·) and second-order (- - - - -) perturbation technique compared with GTD (——) for varying Δ TM case. (a) $\Delta = 1.0$. (b) $\Delta = 2.5$. (c) $\Delta = 5.0$.

In order to more accurately represent an actual riverbed an impedance function with a more gradual transition than the step function was generated and results compared to those generated by the step insert at normal incidence. The transition is made over a distance of $\lambda/2$ and and the width of the gradual impedance function set at 5λ, the same as the step

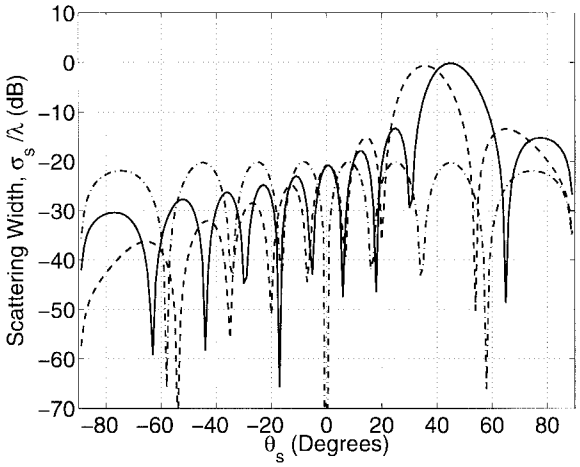

(a)

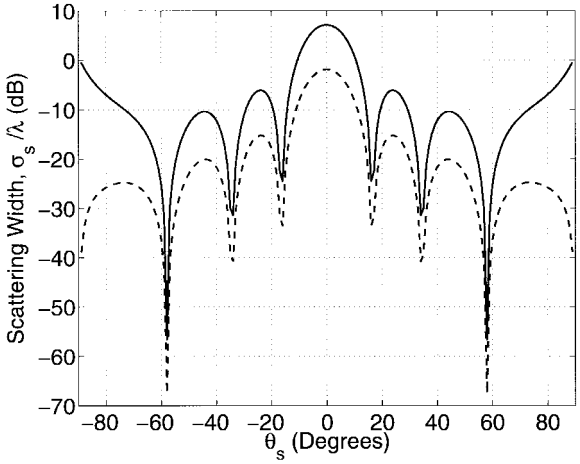

(b)

Fig. 4. Normalized bistatic echo width (σ_s/λ) of an impedance step insert of width 5λ with $\eta_o = 20.9015 - i17.4433, \Delta = 0.5$ at $\theta_i = 45°$, first-order perturbation technique. (a) The effects of obliquity for $\phi_i = 0$ (——), 45 (– – – –), and 90° (· – · –) TM case with (b) cross polarization for $\phi = 90°$, $\mathrm{TE_{TM}}$ (——) and $\mathrm{TM_{TE}}$ (– – – –).

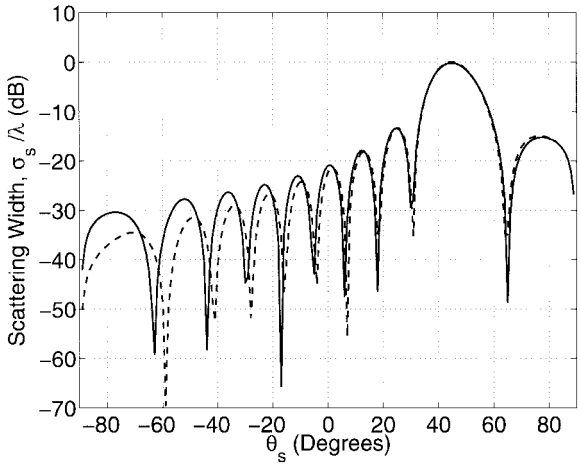

Fig. 5. Normalized bistatic echo width, (σ_s/λ), of an impedance step insert of width 5λ (—) compared with gradual transition insert of bandwidth 5λ (-----), $\eta_o = 20.9015 - i17.4433, \Delta = 0.5$ at $\theta_i = 45°, \phi_i = 0$ for both cases, first-order perturbation technique, TM case.

insert. The width of the gradual impedance function is defined as the distance between points where the function is 3 dB below maximum. Also Δ and η_0 were as set previously for simulated river, or 0.5 and $20.9015 - i17.4433$, respectively. The results for the step insert, shown previously with $\phi_i = 0°$, are overlayed with those of the gradual impedance transition and are shown in Fig. 5 for TM polarization. As can be seen in Fig. 5, the gradual impedance transition tends to lower and pull the sidelobe levels toward the specular scattering direction of $\theta_s = 45°$. This is as expected since a more gradual transition effects the currents less and in the limit should reduce to case of specular scattering only. TE polarization results were similar.

B. Dipole Excitation

The intent of simulation with dipole excitation is to evaluate field strengths as would be expected in a mobile communications channel. With this in mind, a $1/8\lambda$ dipole is placed at a position 1 km away from the impedance step insert along the x axis $(y = 0)$ and 100 m above the impedance plane or at the approximate height of a hill or microwave cellular link. Fig. 2 shows the dipole positioning above the river with Fig. 1 again showing the appropriate axis and angles. Simulations were run for both vertical ($\hat{z}$ directed) and horizontal ($\hat{y}$ directed) dipoles. The E-field strengths are evaluated at a height of 1.8288 m (6 ft) above the impedance plane or approximately the height of a human being. The result of the simulations, for first order diffraction are shown in Fig. 6(a)–(f) with Fig. 6(a)–(c) showing diffracted fields levels in decibels when the impedance plane is excited by a vertically oriented dipole and Fig. 6(d)–(f) showing those excited by a horizontal dipole orientation. The simulations were run for both polarizations with an insert width of $5\lambda, \Delta$ of 0.5 and $\eta_0 = 20.9015 - i17.4433$ as defined previously for an actual river. Results were generated in a $1000 \times 1000\lambda$ grid. The incident field components E_{0x}, E_{0y} were normalized to $(Il)/\lambda$, where I, l are the dipole current amplitude and length as described previously. Due to the far-field criteria that the observation point be at least $2W^2/\lambda$ from the scatterer in the finite dimension, where W is the width of the insert, only results for distances at least 50λ away from the insert are shown. All results within 50λ of the center of the insert are not included and are indicated by the boxed area between 0 and $\pm 50\lambda$ in the x dimension of Fig. 6(a)–(f). For all plots, the dipole is located at a position 100 wavelengths in the $+x$ direction along the $y = 0$ axis, ten wavelengths above the impedance plane ($z_0 = 10\lambda$). The thing to note in Fig. 6(a)–(f) is that the $\hat{z}$ component of the electric field is dominant for either dipole orientation. For the vertically directed dipole the $\hat{z}$ component is two orders of magnitude greater than the $\hat{x}$ component while for a horizontally oriented dipole the $\hat{z}$ component is an order of magnitude greater then the $\hat{y}$ component. Note that a null occurs along the $y = 0$ axis where the dipole is positioned for the $\hat{y}$ field component in the case of the vertical dipole and the $\hat{x}$ and $\hat{z}$ field component for the horizontally oriented dipole, as expected. It is also observed that field levels in the half plane where the dipole is located $(+x)$ are significantly lower than those on the opposite side.

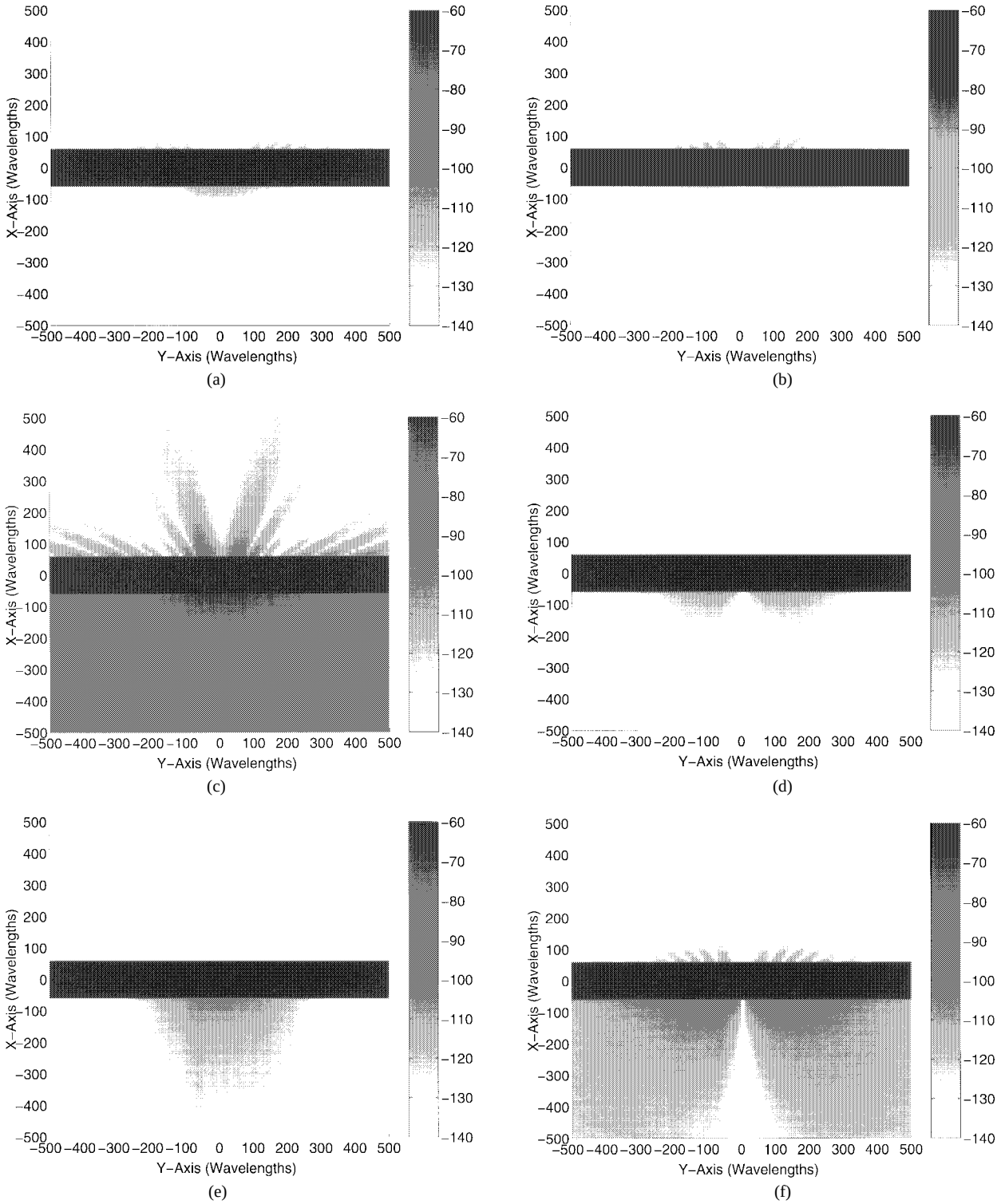

Fig. 6. First-order diffracted E-fields (decibels), vertical, and horizontal dipole excitation for an impedance step insert 5λ wide $\eta_0 = 20.9015 - i17.4433, \Delta = 0.5$. (a) $|E_x|$, (b) $|E_y|$, (c) $|E_z|$ for a vertically oriented dipole with (d) $|E_x|$, (e) $|E_y|$, (f) $|E_z|$ for a horizontally oriented dipole.

Note that the effects of changing receiver heights on diffracted field strength was also investigated. The field levels along the x axis at $y = 0$ were observed for varying receiver heights. In general, received field levels increased for increasing receiver height. This trend was observed for both vertically and horizontally oriented dipole excitations and all receiver field polarizations with one exception. The $\hat{y}$-field component generated by a vertically oriented dipole showed a decrease in field levels for increasing receiver heights.

VII. Conclusions

The intent of this study was to accurately predict and observe diffraction from terrain features that can be modeled by variable impedance surfaces such as rivers, flat shorelines,

and shallow troughs. Using the field equivalence principle, the diffraction problem is formulated in terms of an integral equation for a fictitious electric current induced on the variable impedance surface. The river was modeled as an impedance transition in an infinite plane. A perturbation technique was used to derive a recursive solution for any order diffraction current in terms of the previous order. Stationary phase techniques were used to evaluate far-field expressions for both plane wave and short dipole excitations. Initial results were shown for plane wave excitation to characterize and validate the perturbation technique. Error bounds were established to show that the technique could evaluate perturbations equivalent to those of an actual river. Using impedances comparable to those of an actual river, scattering results, at various oblique incidence angles, were shown when the impedance transition was a step function. It was observed that the cross-polarization levels for a TM polarized field incident along the river dominated the scattering levels. Effects of a more realistic gradual impedance transition were also shown. Results were then generated for short dipole excitation. It was observed that the $\hat{z}$ component of the received electric fields dominated for either a vertically or horizontally oriented dipole and increasing receiver height produced higher field levels for most cases.

REFERENCES

[1] M. Lebherz, W. Wiesbeck, and W. Krank, "A versatile wave propagation model for the VHF/UHF range considering three-dimensional terrain," *IEEE Trans. Antennas Propagat.*, vol. 40, pp. 1121–1131, Oct. 1992.

[2] T. Kürner, D. J. Cichon, and W. Wiesbeck, "Concepts and results for 3-D digital terrain-based wave propagation models: An overview," *IEEE J. Selected Areas Commun.*, vol. 11, pp. 1102–1012, Sept. 1993.

[3] ———, "Evaluation and verification of the VHF/UHF propagation channel based on a 3-D-wave propagation model," *IEEE Trans. Antennas Propagat.*, vol. 44, pp. 393-404, Mar. 1996.

[4] S. R. Saunders and F. R. Bonar, "Prediction of mobile radio wave propagation over buildings of irregular heights and spacings," *IEEE Trans. Antennas Propagat.*, vol. 42, pp. 137–143, Feb. 1994.

[5] J. Bazer and S. N. Karp, "Propagation of plane electromagnetic waves past a shoreline," *J. Res. (Nat. Bur. Std.)*, vol. D66, pp. 319–334, 1962.

[6] J. R. Wait, "Recent analytical investigations of electromagnetic ground wave propagation over inhomogeneous Earth models," *Proc. IEEE*, vol. 62, pp. 1061–1072, Aug. 1974.

[7] G. de Jong, "Electromagnetic wave propagation over an inhomogeneous flat Earth (two-dimensional integral equation formulation)," *Radio Sci.*, vol. 10, pp. 925–933, 1975.

[8] R. H. Ott, "RING: An integral equation algorithm for HF-VHF radio wave propagation over irregular, inhomogeneous terrain," *Radio Sci.*, vol. 27, 867–882, 1992.

[9] K. Sarabandi, "Scattering from variable resistive and impedance sheets," *J. Electromagn. Waves Applicat.*, vol. 4, pp. 865–891, 1990.

[10] M. I. Herman and J. L. Volakis, "High frequency scattering from polygonal impedance cylinders and strips," *IEEE Trans. Antennas Propagat.*, vol. 36, pp. 679–688, May 1988.

[11] R. F. Harrington, *Time-Harmonic Electromagnetic Fields*. New York: McGraw-Hill, p. 317, 1961.

[12] L. Tsang, J. A. Kong, and R. T. Shin, *Theory of Microwave Remote Sensing*. New York: Wiley, 1985, pp. 32–34.

[13] J. W. Goodman, *Introduction to Fourier Optics*. New York: McGraw-Hill, 1968, p. 278.

[14] J. D. Murray, *Asymptotic Analysis*. New York: Springer-Verlag, 1984, pp. 72–85.

[15] V. A. Borovikov, *Uniform Stationary Phase Method*. London, U.K.: IEE, 1994, pp. 79–82.

[16] F. T. Ulaby, R. K. Moore, and A. K. Fung, *Microwave Remote Sensing, Active and Passive—Vol. III: From Theory to Applications*. Norwood, MA: Artech House, 1986, pp. 2022–2025.

[17] J. E. Hipp, "Soil electromagnetic parameters as functions of frequency, soil density, and soil moisture," *Proc. IEEE*, vol. 62, pp. 98–103, Jan. 1974.

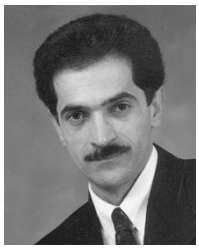

Kamal Sarabandi (S'87–M'90–SM'92) received the B.S. degree in electrical engineering from Sharif University of Technology, Tehran, Iran, in 1980, and the M.S.E. (electrical engineering), M.S. (mathematics), and Ph.D. degrees (electrical engineering) all from the University of Michigan, Ann Arbor, in 1986 and 1989 (M.S. and Ph.D.), respectively.

From 1980 to 1984, he worked as a Microwave Engineer in the Telecommunication Research Center. He is presently an Associate Professor in the Department of Electrical Engineering and Computer Science at the University of Michigan. He has 15 years of experience with microwave sensors and radar systems. In the past eight years he has served as the Principal Investigator and Co-Investigator on many projects sponsored by National Aeronautic Space Administration (NASA), Jet Propulsion Laboratory (JPL), Army Research Office (ARO), Office of Naval Research (ONR), and General Motors (GM), all related in one way or another to microwave and millimeter-wave radar remote sensing. He has published many book chapters and more than 70 papers in refereed journals on electromagnetic scattering, random media modeling, microwave measurement techniques, radar calibration, application of neural networks in inverse scattering problems, and microwave sensors. He has also had more than 130 papers and invited presentations in national and international conferences and symposia on similar subjects.

Dr. Sarabandi is a member of the IEEE Geoscience and Remote Sensing ADCOM since January 1998 and served as the Chairman of Geoscience and Remote Sensing Society Southeastern Michigan Chapter from 1991 to 1997. He is also a member of Commission F of URSI and of The Electromagnetic Academy. He was a recipient of a 1996 Teaching Excellence Award, the 1997 Henry Russel Award from the Regent of The University of Michigan, and the 1999 GAAC Distinguished Lecturer Award from the German Federal Ministry for Education, Science, and Technology. He is listed in *American Men & Women of Science* and *Who's Who in Electromagnetics*.

Mark D. Casciato (S'86–M'89) was born in New Castle, PA, in June 1956. He received the B.S.E.E. and M.S.E.E. degrees, both from Florida Atlantic University, Boca Raton, FL, in 1988 and 1995, respectively. He is currently working toward the Ph.D. degree at the University of Michigan, Ann Arbor.

From 1989 to 1992, he worked as an RF/Microwave Design Engineer at Allied Signal Aerospace, Ft. Laurderdale, FL. In the summer of 1995 he interned at MIT-Lincoln Laboratory/Group 34, Cambridge, MA, working in the area of electromagnetic scattering prediction. Since September 1995 he has worked as a Graduate Research Assistant with the Radiation Laboratory, University of Michigan. His current research interests include electromagnetic scattering and diffraction techniques as applied to radio wave propagation and radar.